14th International Symposium on Turbulence and Shear Flow Phenomena (TSFP14)
Heidelberg, Germany, July 28–31, 2026

CONTRIBUTION FROM LINEAR AMPLIFICATION TO DRAG REDUCTION FROM RIBLETS

Stephen J Terrington
D. Mech. Eng.
University of Melbourne
Melbourne, VIC 3010, Australia
stephen.terrington@unimelb.edu.au

Christopher J Camobreco
D. Mech. Eng.
University of Melbourne
Melbourne, VIC 3010, Australia
christopher.camobreco@unimelb.edu.au

Mitul Luhar
D. Aero. Mech. Eng.
University of Southern California
Los Angeles, CA 90089, USA
luhar@usc.edu

Nicholas Hutchins
D. Mech. Eng.
University of Melbourne
Melbourne, VIC 3010, Australia
nhu@unimelb.edu.au

Daniel Chung
D. Mech. Eng.
University of Melbourne
Melbourne, VIC 3010, Australia
daniel.chung@unimelb.edu.au

ABSTRACT

Resolvent analysis has emerged as a promising tool to predict the drag reduction performance of riblets. However, its predictive capability has not been validated in detail. Here, we compare resolvent analysis to time-resolved direct numerical simulations (DNSs) of turbulent flow over blade riblets, both near and beyond the optimal size. The DNSs show that the turbulent kinetic energy and Reynolds shear stress spectra are essentially smooth-wall like for riblets near the optimal size, as expected. For riblets larger than the optimal size, shorter quasi-streamwise vortex structures are more energetic compared to the smooth wall, and increase drag, while longer near-wall streak structures are less energetic compared to the smooth wall, and reduce drag. Both of these changes are mirrored in the gain of the resolvent operator, which represents the linear amplification or damping of turbulent fluctuations by the mean flow. Thus, the departure of turbulence from smooth-wall likeness is at least partly explained by changes to the linear amplification mechanisms, which can be predicted using the resolvent operator.

INTRODUCTION

Skin-friction drag of turbulent boundary layers can be reduced via the application of small spanwise-repeating surface textures, known as riblets (García-Mayoral & Jiménez, 2011). Riblet drag reduction performance is characterised by the geometric parameter ℓ_g^+ (García-Mayoral & Jiménez, 2011), which is the square-root of the groove area in viscous units. Figure 1(a) shows the drag reduction (characterised by the shift in mean velocity profile compared to a smooth wall ΔU^+) against ℓ_g^+ reported by Wong *et al.* (2024) for blade riblets, with thickness-to-spacing ratio $t_r/s = 0.2$ and height-to-spacing ratio $k/s = 0.5$. Maximum drag reduction, indicated by a negative value of ΔU^+, occurs for $\ell_g^+ \approx 10.7$, and this optimum value of ℓ_g^+ holds for a wide variety of riblet geometries (García-Mayoral & Jiménez, 2011).

Riblet drag reduction is due to a difference in the virtual origins of the mean flow (ℓ_U) and turbulence (ℓ_T). Based on this principle, Wong *et al.* (2024) developed a viscous vortex model to predict drag reduction, which is presented in figure 1(a). This model accurately predicts the drag reduction for riblets up to the optimum size $\ell_g^+ \lesssim 10$, as the flow is essentially smooth-wall like aside from the shift in virtual origins. However, it does not predict the breakdown of drag reduction for larger, post-optimal riblets.

The mechanisms leading to the breakdown of drag reduction for large riblets are still not well understood. García-Mayoral & Jiménez (2011) proposed that a Kelvin–Helmholtz-type instability can explain the loss of drag reduction, but recent work (Endrikat *et al.*, 2021; Camobreco *et al.*, 2025) showed that this instability cannot explain the loss of drag reduction for all riblet geometries. Modesti *et al.* (2021) linked the loss of drag reduction to dispersive stresses due to the time-averaged spanwise and wall-normal flow, and changes to the turbulent stresses, but did not provide a causal mechanism. A restricted nonlinear model (Zhu *et al.*, 2025), which omits some interscale nonlinear interactions, can accurately predict the total drag reduction.

One promising candidate to understand the loss of drag reduction is resolvent-based analysis (Chavarin & Luhar, 2020). In resolvent analysis, the nonlinear terms in the Navier–Stokes equations are interpreted as an external forcing, which are amplified by linear mechanisms (McKeon & Sharma, 2010). Chavarin & Luhar (2020) computed the gain of the resolvent operator – representing the maximum possible amplification by the linear terms – for riblets of various sizes, and observed that the variation in gain closely matches the drag reduction curve. Figure 1(b) shows the gain of a mode representative of the near-wall streaks for the blade riblets considered in figure 1(a). The variation in gain closely matches the drag reduction curve, with a local minimum in gain occurring between $\ell_g^+ = 9.9$ and $\ell_g^+ = 12.8$. However, the details of this apparent relationship between resolvent gain and drag reduction remain elusive.

Using a similar linear input-output analysis, Ran *et al.* (2021) obtain drag reduction predictions in reasonable agreement with existing experimental and numerical data, further demonstrating the potential of linear input-output analysis to model drag reduction. There, they first estimate the mean ve-

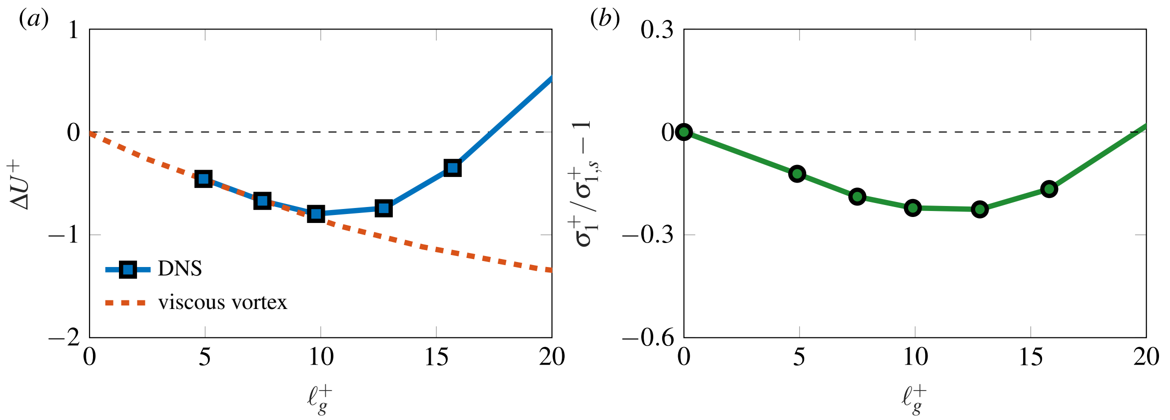

Figure 1. (a) Comparison between the velocity difference ΔU^+ from DNS and the viscous vortex model for blade riblets ($t_r/s = 0.2$, $k/s = 0.5$) reproduced from Wong *et al.* (2024). (b) Variation of resolvent gain σ_1^+ normalised by the smooth-wall value $\sigma_{1,s}^+$ against riblet size ℓ_g^+ for a mode with streamwise wavelength $\lambda_x^+ = 1000$, spanwise wavelength $\lambda_y^+ = 120$ and wavespeed $c^+ = 10$.

Table 1. Simulation cases from Endrikat *et al.* (2021) and Wong *et al.* (2024), which were extended to collect time-resolved data. Here, s^+ is the riblet spacing, ℓ_g^+ the square-root of the groove area, Δt^+ the sampling period and N_t the number of snapshots.

Case		s^+	ℓ_g^+	Δt^+	N_t
BL16	blade riblet	15.6	9.9	2.37	27,000
BL20	blade riblet	20.3	12.8	2.37	27,000
BL25	blade riblet	25.0	15.8	2.37	35,000
S395	smooth wall			2.37	30,000

locity profile using a Cess eddy-viscosity model, then use the stochastically forced linearised equations to obtain a modified eddy viscosity to predict the drag reduction.

The present study compares in detail the predictions of resolvent analysis to time-resolved DNS of turbulent flow over blade riblets, to provide insight into the relationship between linear amplification and drag reduction. We identify changes to the turbulent kinetic energy and Reynolds shear stress spectra which occur for large riblets, compared to the smooth-wall spectra, and investigate whether these changes are reflected in the gain of the resolvent operator.

DIRECT NUMERICAL SIMULATIONS

We consider turbulent flow in a minimal channel at $Re_\tau = 395$. We use a Cartesian coordinate system with (x,y,z) the streamwise, spanwise and wall-normal coordinates, respectively, and $z = 0$ at the riblet crest. A Reynolds decomposition is performed, with $(U,V,W) = \boldsymbol{U}(\tilde{y},z)$ and $(u,v,w) = \boldsymbol{u}(x,y,z,t)$ being the mean and fluctuating velocities, respectively. The coordinate $\tilde{y}$ is the spanwise position restricted to a single riblet period ($y = \tilde{y} + ps$, where p is the riblet index and s the riblet spacing), and the mean flow is averaged over time t, streamwise coordinate x, and riblet index p. Viscous-friction scaled variables are denoted by a superscript $^+$.

A selection of cases from our previous studies (Endrikat *et al.*, 2021; Wong *et al.*, 2024) listed in table 1 are extended to collect time-resolved data. These include three blade riblets ($\ell_g^+ = 9.9, 12.8, 15.8$) and a smooth-wall reference case. The sampling resolution for time-resolved data was $\Delta t^+ = 2.37$ for all cases, and approximately 30,000 snapshots (representing a time-interval of $L_t^+ = 70{,}000$) are collected for each case. Simulations are performed in a minimal channel with spanwise width $L_y^+ \approx 250$ and streamwise length $L_x^+ \approx 1000$. Due to the use of a minimal channel, simulation results are only accurate below a height of $z^+ \approx 100$, and results for larger wall-normal distances are not presented. For further details on the numerical simulations, refer to Endrikat *et al.* (2021) and Wong *et al.* (2024).

Virtual origin of turbulence

For small riblets, the turbulence is essentially smooth-wall like, but shifted in the wall-normal direction with a virtual origin at $z + \ell_T = 0$ (Gómez-de Segura *et al.*, 2018). For larger riblets, the turbulence is modified near the wall, but remains similar in the outer layer after a wall-normal shift, somewhat similar to the virtual origin concept, but historically called the zero-plane displacement. Here, this zero-plane displacement is estimated by minimising the mean-squared error in the $\langle uw \rangle$ Reynolds stress profiles between the rough and smooth walls over the range $10 \le z^+ + \ell_T^+ \le 100$. Quantities in viscous units are normalised using an effective friction velocity u_τ based on the virtual turbulence origin $z + \ell_T = 0$ (Wong *et al.*, 2024).

Figure 2(a) shows the Reynolds shear stress and turbulent kinetic energy profiles, respectively, after shifting by ℓ_T^+. The Reynolds shear stress profiles collapse well away from the wall ($z^+ + \ell_T^+ \gtrsim 10$) for all riblet sizes, however the Reynolds stress magnitudes are larger near the wall for the larger riblets. Unlike the Reynolds stress profiles, the turbulent kinetic energy profiles (figure 2b) do not collapse onto the smooth-wall profile for riblets larger than the optimal size.

Figure 2(c) shows that the mean streamwise velocity profiles collapse well away from the wall after shifting by both ℓ_T^+ and ΔU^+, where ΔU^+ is measured by averaging over $50 \le z^+ + \ell_T^+ \le 100$. Near the riblet crests, however, slightly higher mean velocities are observed for larger riblets.

Reynolds stress spectra

We now compare the kinetic energy and Reynolds shear stress spectra between the blade riblets and the smooth wall. Time-based spectra are estimated using the Welch method,

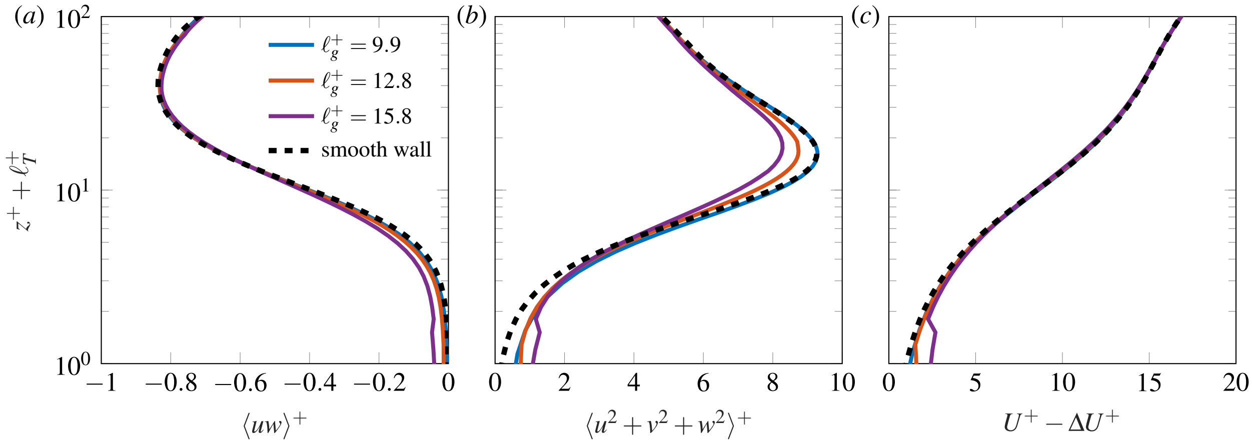

Figure 2. Profiles of (*a*) Reynolds shear stress and (*b*) turbulent kinetic energy after accounting for the virtual turbulence origin ℓ_T^+, and (*c*) mean streamwise velocity profiles after accounting for the shifts in mean velocit ΔU^+ and turbulence origin ℓ_T^+.

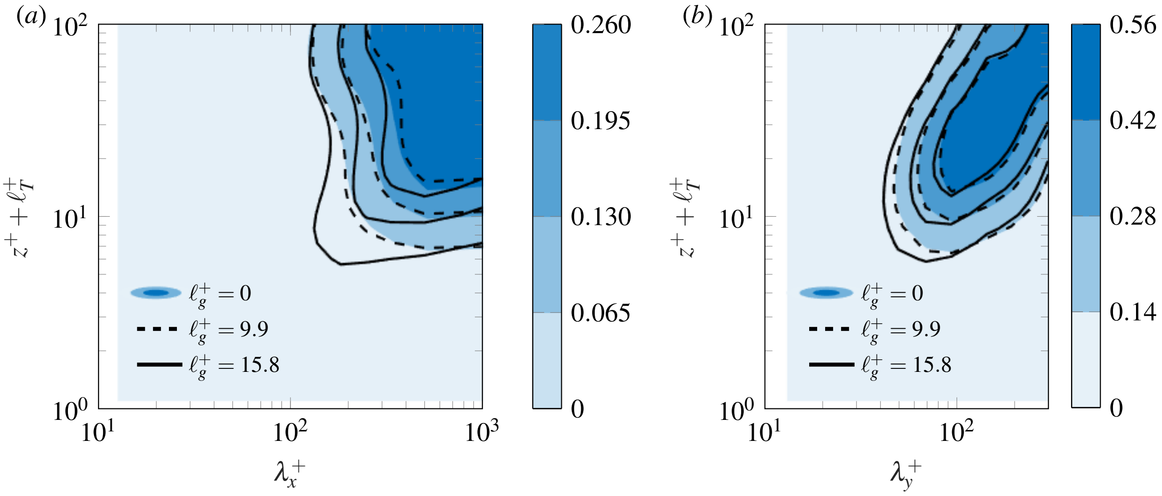

Figure 3. Comparison between (*a*) κ_x^+-premultiplied and (*b*) κ_y^+-premultiplied S_{uw}^+ Reynolds stress spectra integrated over all ω^+ and (*a*) κ_y^+ or (*b*) κ_x^+, for a smooth wall (filled contours) and blade riblets with $\ell_g^+ = 9.9$ (dashed lines) and $\ell_g^+ = 15.8$ (solid lines).

with $N = 1028$ snapshots per block and 50% overlap between blocks. Spectral densities S_{uw} are normalised as

$$\langle uw \rangle = \int_{-\infty}^{\infty}\int_{-\infty}^{\infty}\int_{-\infty}^{\infty} S_{uw}(z, \kappa_x, \kappa_y, \omega)\,\mathrm{d}\omega\,\mathrm{d}\kappa_x\,\mathrm{d}\kappa_y \qquad (1)$$

Continuous spectra are approximated from the discrete spectra using linear interpolation, and continuous integrals are evaluated using the procedure outlined in §A.3.3 of Endrikat (2020).

Figure 3 shows the S_{uw} spectra for the smooth wall (filled contours) and blade riblets with $\ell_g^+ = 9.9$ (dashed lines) and $\ell_g^+ = 15.8$ (solid lines). The spectra for the $\ell_g^+ = 9.9$ riblets is relatively smooth-wall like. However, above the larger riblets ($\ell_g^+ = 15.8$) there is an increased Reynolds stress contribution from small wavelengths ($\lambda_x^+ \approx 200$, $\lambda_y^+ \approx 60$), which is most significant between $z^+ + \ell_T^+ = 5$ and 25.

To identify which wavelengths contribute most to increased drag, we compute the difference in Reynolds stresses compared to a smooth wall over the range $5 \le z^+ + \ell_T^+ \le 25$,

$$D = \int_5^{25}\int_{-\infty}^{\infty} [S_{uw,s}^+(z^+) - S_{uw,r}^+(z^+ + \ell_T^+)]\,\mathrm{d}\omega\,\mathrm{d}z^+ \qquad (2)$$

where subscripts s and r denote the smooth-wall and riblet case, respectively. A positive D indicates a drag-increasing change to the Reynolds stresses, while a negative D indicates a drag reducing change (Modesti *et al.*, 2021).

Figure 4 presents these integrated stress differences for two different riblet sizes. These differences are relatively small for the $\ell_g^+ = 9.9$ riblets, but are more pronounced for the larger $\ell_g^+ = 15.8$ riblets. There is a drag-increasing D for small wavelengths, with a maximum value at approximately $\lambda_x^+ = 200$ and $\lambda_y^+ = 60$ (green circles). There is also a drag-reducing contribution at wavelengths representative of near-wall streaks, with a minimum value near $\lambda_x^+ \approx 1000$ and $\lambda_y^+ = 120$ (purple triangles). A spanwise-roller instability with $\lambda_x^+ \approx 150$ and $\lambda_y^+ = \infty$ (orange diamonds) is also known to occur for larger post-optimal riblets (García-Mayoral & Jiménez, 2011). In figure 4(*b*), spanwise rollers with $\lambda_x^+ \lesssim 200$ are drag reducing, while Endrikat *et al.* (2021) reported a small drag increase from spanwise rollers for the same $\ell_g^+ = 15.8$ blade riblets. This discrepancy is likely due to the different definition of ℓ_T^+ used, and in either case the drag reduction or increase from spanwise rollers is small for these riblets.

The spectral densities of kinetic energy $S_{E_k} = S_{uu} + S_{vv} + S_{ww}$ and Reynolds shear stress S_{uw} are presented in figure 5 for wavenumbers representative of (*a-c*) spanwise rollers, (*d-*

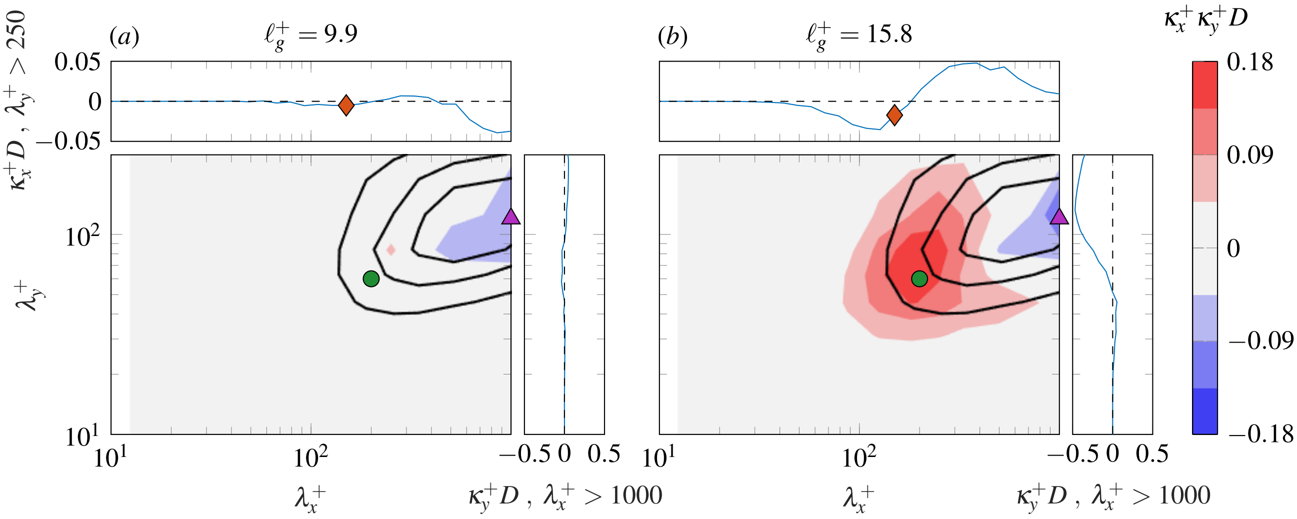

Figure 4. Differences in the S_{uw} Reynolds stress spectra between the smooth wall and blade riblets with (*a*) $\ell_g^+ = 9.9$ and (*b*) $\ell_g^+ = 15.8$, integrated over $5 \le z^+ + \ell_T^+ \le 25$ (equation 2). Positive (red) corresponds to drag-increasing, while negative (blue) indicates drag reducing. Line plots show the integrated contributions from large spanwise ($\lambda_y^+ > 250$; top) and streamwise ($\lambda_x^+ > 1000$; right) wavelengths, respectively. Markers indicate three modes of interest: spanwise-infinite rollers ($\lambda_x^+ = 150$, $\lambda_y^+ = \infty$; ◆), a drag-increasing structure ($\lambda_x^+ = 200$, $\lambda_y^+ = 60$; ●) and a drag-reducing structure ($\lambda_x^+ = 1000$, $\lambda_y^+ = 120$; ▲).

f) a shorter drag increasing structure and (*g*-*i*) a longer drag-reducing structure. Spectra are plotted against wavespeed $c^+ - \Delta U^+$ and wall-normal position $z^+ + \ell_T^+$, and are premultiplied by κ_x^+ to account for the change in variables from ω to c^+.

The spanwise-roller instability is evident in figure 5(*a*,*b*), with a peak in kinetic energy near $c^+ = 6$ and $z^+ + \ell_T^+ < 10$ for the blade riblet spectra which is absent from the smooth-wall spectra. However, regions of both drag increase and drag decrease are evident in figure 5(*c*) so the total contribution to the change in drag is small.

The shorter drag-increasing structure is more energetic above blade riblets than above a smooth wall (figures 5*d*,*e*), with differences greatest near $c^+ - \Delta U^+ = 9$ and $z^+ + \ell_g^+ = 10$. The increased energy of these structures also corresponds to a drag-increasing change to the $\langle uw \rangle$ Reynolds stresses (figure 5*f*). In contrast, the blade riblets contain less energy at wavelengths typical of near-wall streaks (figure 5*g*,*h*), with differences greatest at $c^+ - \Delta U^+ = 11$ and $z^+ + \ell_T^+ = 10$. This corresponds to a negative (drag-decreasing) change to the $\langle uw \rangle$ Reynolds stresses (figure 5*i*).

RESOLVENT ANALYSIS

Resolvent analysis is typically performed using the Fourier-transformed linearised Navier–Stokes equations (McKeon & Sharma, 2010). However, to account for the spanwise periodicity of riblets, we instead perform a Floquet–Bloch transform in the spanwise direction,

$$\tilde{u}(\tilde{y}, z, \kappa_x, \kappa_y, \omega) = \frac{1}{N_r L_x L_t} \sum_{p=0}^{N_r - 1} \int_0^{L_x} \int_0^{L_t} u(x, y, z, t) \mathrm{e}^{-\mathrm{i}(\kappa_x x + \kappa_y y - \omega t)} \mathrm{d}x \mathrm{d}t \qquad (3)$$

where $y = \tilde{y} + ps$. Transformed variables are periodic in $\tilde{y}$ ($0 \le \tilde{y} < s$), and the spanwise wavenumbers are restricted to $-\pi/s \le \kappa_y < \pi/s$. The Floquet–Bloch transformed Navier–Stokes equations, linearised about the mean flow $\boldsymbol{U}(\tilde{y}, z)$, are then expressed as $\tilde{\boldsymbol{q}} = \boldsymbol{R}\tilde{\boldsymbol{f}}$, where $\tilde{\boldsymbol{q}} = (\tilde{u}, \tilde{v}, \tilde{w}, \tilde{p})$ is a vector of state variables, the resolvent operator $\boldsymbol{R}$ represents the linear terms and $\tilde{\boldsymbol{f}}$ are the nonlinear terms. The nonlinear terms are interpreted as an external forcing, which are amplified by linear mechanisms.

The most-amplified mode is determined by performing a singular-value decomposition of the resolvent operator (McKeon & Sharma, 2010; Chavarin & Luhar, 2020). Weight matrices are introduced, so the singular values σ_j are sorted by the amplification of kinetic energy, with σ_1 being the gain of the most amplified mode. We use the approach of Garnaud *et al.* (2013) to obtain the singular values, implemented using the finite element software FreeFem (Hecht, 2012). This code was validated against the method of Chavarin & Luhar (2020). Previously, Chavarin & Luhar (2020) modelled the mean flow using an eddy-viscosity approximation, while here we linearise the Navier–Stokes equations about the mean flow extracted from DNS.

Effect of riblets on resolvent gain

Figure 6 plots the variation in gain against wavespeed c^+ for wavelengths corresponding to (*a*) a shorter drag-increasing structure and (*b*) a longer drag-reducing structure. Here, wavespeeds are shifted by the shift in mean streamwise velocity ΔU^+, so that the curves collapse at high wavespeeds.

For the drag-increasing quasi-streamwise vortex (figure 6*a*), there is an increase in gain compared to the smooth wall for $c^+ - \Delta U^+ \lesssim 12$, indicating that, in addition to the change in advection velocity, these structures are also more amplified by linear interactions with the mean flow. This is consistent with the DNS kinetic energy spectra (figure 5*e*), where this mode was found to be more energetic for blade riblets compared to the smooth wall. For the drag-reducing near-wall streak (subfigure 6*b*), the gain is slightly reduced compared to the smooth wall at $c^+ - \Delta U^+ \approx 10$, in agreement with the change in kinetic energy observed from the DNS spectra for this mode (figure 5*h*).

The insets in figure 6 show the change in gain against ℓ_g^+ for either a fixed c^+ (green circles) or fixed $c^+ - \Delta U^+$ (or-

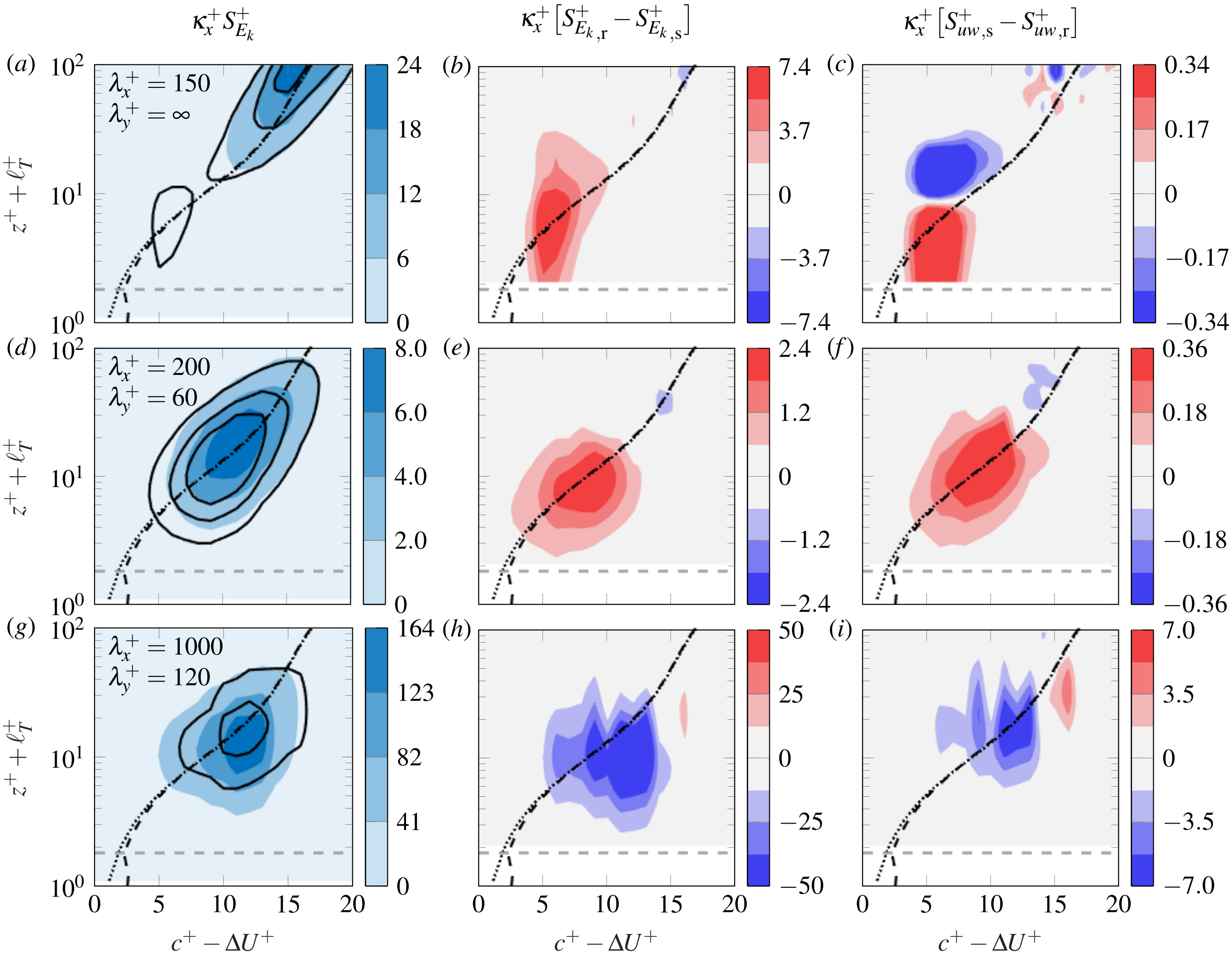

Figure 5. Comparison between the spectral densities of kinetic energy and $\langle uw \rangle$ Reynolds stress for $\ell_g^+ = 15.8$ blade riblets and the smooth wall, plotted against $c^+ - \Delta U^+$ and $z^+ - \ell_T^+$ for wavenumbers representative of (*a-c*) spanwise rollers, $\lambda_x^+ = 150$ and $\lambda_y^+ = \infty$; (*d–f*) a shorter drag-increasing structure, $\lambda_x^+ = 200$ and $\lambda_y^+ = 60$; and (*g–i*) a longer drag-decreasing structure, $\lambda_x^+ = 1000$ and $\lambda_y^+ = 120$. Panels (*a,d,g*) plot the kinetic energy spectral density ($S_{E_k}^+$) for both the smooth wall (colour contours) and riblets (solid lines); (*b,e,h*) plot the difference between the blade riblet and smooth wall kinetic energy spectra, with red indicating an increase in kinetic energy for riblets; (*c,f,i*) plot the difference between the blade riblet and smooth wall Reynolds stress spectra, with red indicating a drag increase for riblets. Spectra are smoothed by averaging with a window size $\Delta c^+ = 1$. The black dashed and dotted lines are the mean streamwise velocities for blade riblets and smooth wall, respectively, while the grey dashed line denotes the riblet crest height.

ange squares). Changes to the gain at a fixed c^+ are largely due to changes in the mean advection velocity, particularly for the near-wall streaks (figure 6*b*), where the gain at a fixed $c^+ - \Delta U^+$ is relatively constant. This explains the similar trends in σ_1^+ and ΔU^+ observed by Chavarin & Luhar (2020). By comparison, plotting the gain for a fixed $c^+ - \Delta U^+$ better reflects the changes to the turbulence kinetic energy observed in the DNS spectra, where drag-increasing structures are more energetic, and drag-reducing structures are less energetic.

Figure 7(*a*) shows the smooth-wall gain (filled contours) against λ_x^+ and λ_y^+ for $c^+ = 10$, as well as contours of turbulence kinetic energy spectra (solid lines) measured from DNS. The resolvent gain does not correspond well to the DNS TKE spectra, since the nonlinear forcing term $\tilde{\boldsymbol{f}}$ has not been considered. However, the ratio of gain for blade riblets compared to smooth wall (figure 7*b-d*) compares favourably with the changes to the Reynolds shear stresses seen in the DNS (figure 4). The gain at longer streamwise wavelengths is reduced, while the gain at shorter wavelengths is increased. The large gain near $\lambda_y^+ = 2s^+$ is likely an artefact of the mathematical transformations used, and not physically significant.

CONCLUSIONS

From time-resolved DNS data, we identified changes to the turbulence kinetic energy and $\langle uw \rangle$ Reynolds stress spectra above large ($\ell_g^+ > 10$) blade-type riblets, relative to the smooth wall. Near-wall streaks ($\lambda_x^+ = 1000$, $\lambda_y^+ = 120$) were less energetic compared to the smooth wall, and reduced drag, while shorter quasi-streamwise vortices ($\lambda_x^+ = 200$, $\lambda_y^+ = 60$) were more energetic compared to the smooth wall, and increased drag. These changes were reflected in the gain of the resolvent operator, which describes the linear amplification of turbulence by the mean flow. Thus, changes to the turbulence spectra are explained at least partly by changes to linear amplification mechanisms, which can be predicted using resolvent analysis.

This work was supported by AFOSR award FA2386-23-1-4071 (PM: David Newell), by the Australian Government DISR project CRCPXIV000025, and by computational re-

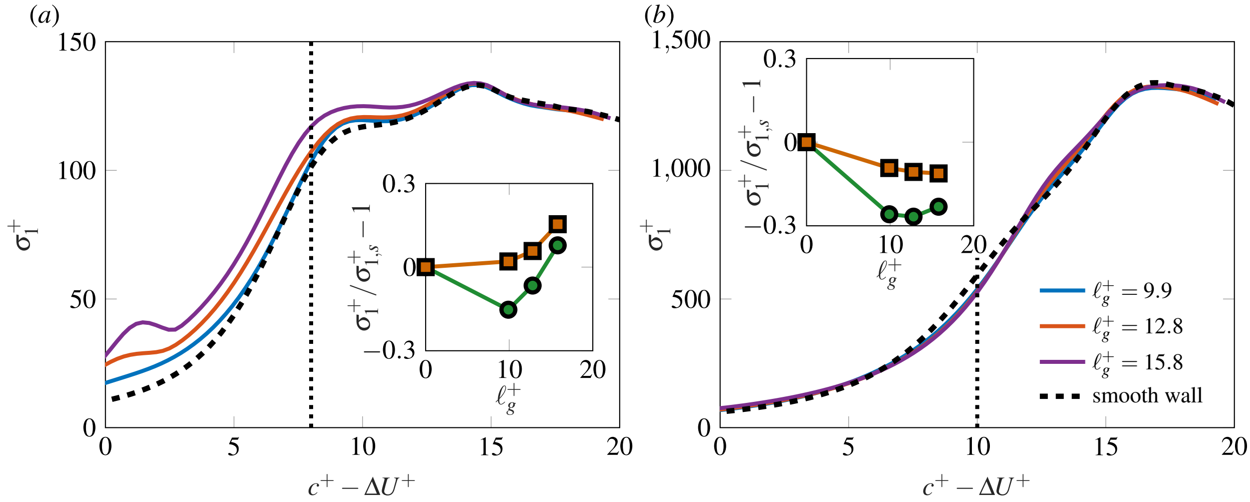

Figure 6. Variation of resolvent gain σ_1^+ against wavespeed c^+ accounting for the shift in mean flow velocity ΔU^+, for both the smooth wall and three different sizes of blade riblets, for (*a*) $\lambda_x^+ = 200$ and $\lambda_y^+ = 60$ and (*b*) $\lambda_x^+ = 1000$, $\lambda_y^+ = 120$. Insets show the variation in gain with respect to ℓ_g^+ at either a fixed c^+ (circles) or fixed $c^+ - \Delta U^+$ (squares) of (*a*) 8 and (*b*) 10.

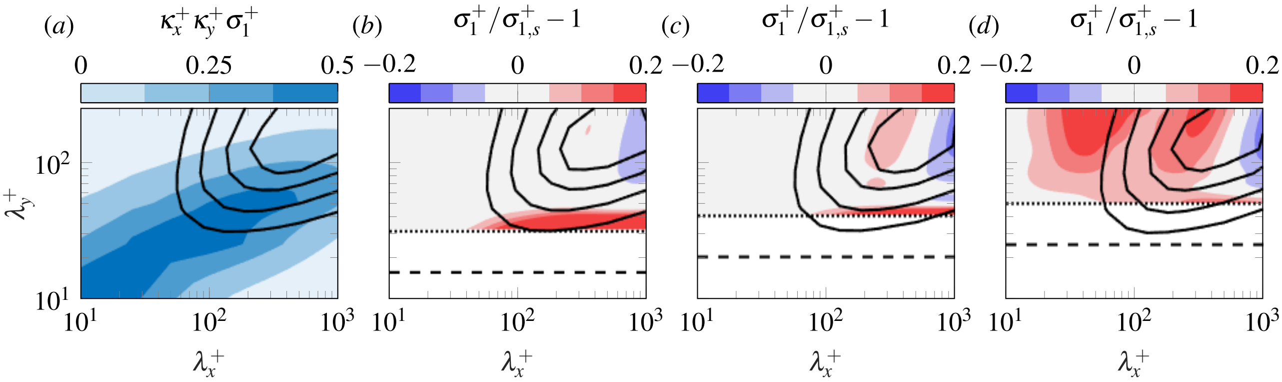

Figure 7. (*a*) Variation of premultiplied resolvent gain against λ_x^+ and λ_y^+ for the smooth wall at $c^+ = 10$, and (*b-d*) the ratio between the resolvent gain for blade riblets compared to the smooth wall at $c^+ = 10$, for (*b*) $\ell_g^+ = 9.9$, (*c*) $\ell_g^+ = 12.8$ and (*d*) $\ell_g^+ = 15.8$. Solid black lines are contours of kinetic energy spectra from DNS data, $\int_5^{100} \int_{-\infty}^{\infty} S_{E_k}^+ \mathrm{d}\omega^+ \mathrm{d}z^+$, at 10%, 25%, 50% and 75% of the maximum value for the smooth wall. The black dashed and dotted lines indicate $\lambda_y^+ = s^+$ and $\lambda_y^+ = 2s^+$, respectively.

sources provided through the Research Computing Services of the University of Melbourne and through the Australian Government's National Computational Merit Allocation Scheme. ML was supported by NSF award 1943105 and ONR award N00014-22-1-2029 (PM: Dr. Leighton Myers).

REFERENCES

Camobreco, C. J., Endrikat, S., García-Mayoral, R., Luhar, M. & Chung, D. 2025 Why do only some riblets promote spanwise rollers? *J. Fluid Mech.* **1022**, A35.

Chavarin, A. & Luhar, M. 2020 Resolvent analysis for turbulent channel flow with riblets. *AIAA J.* **58**, 589–599.

Endrikat, S. 2020 Effects of riblet shape on drag reduction in turbulent flow. PhD thesis, University of Melbourne.

Endrikat, S., Modesti, D., García-Mayoral, R., Hutchins, N. & Chung, D. 2021 Influence of riblet shapes on the occurrence of Kelvin–Helmholtz rollers. *J. Fluid Mech.* **913**, A37.

García-Mayoral, R. & Jiménez, J. 2011 Drag reduction by riblets. *Phil. Trans. R. Soc. A.* **369**, 1412–1427.

Garnaud, X., Lesshafft, L., Schmid, P. J. & Huerre, P. 2013 The preferred mode of incompressible jets: linear frequency response analysis. *J. Fluid Mech.* **716**, 189–202.

Hecht, F. 2012 New development in FreeFem++. *J. Numer. Math.* **20**, 251–266.

McKeon, B. J. & Sharma, A. S. 2010 A critical-layer framework for turbulent pipe flow. *J. Fluid Mech.* **658**, 336–382.

Modesti, D., Endrikat, S., Hutchins, N. & Chung, D. 2021 Dispersive stresses in turbulent flow over riblets. *J. Fluid Mech.* **917**, A55.

Ran, W., Zare, A. & Jovanović, M. R. 2021 Model-based design of riblets for turbulent drag reduction. *J. Fluid Mech.* **906**, A7.

Gómez-de Segura, G., Sharma, A., García-Mayoral, R., Moin, P. & Urzay, J. 2018 Virtual origins in turbulent flows over complex surfaces. *CTR2018* pp. 277–286.

Wong, J., Camobreco, C. J., García-Mayoral, R., Hutchins, N. & Chung, D. 2024 A viscous vortex model for predicting the drag reduction of riblet surfaces. *J. Fluid Mech.* **978**, A18.

Zhu, X., Viggiano, B., Minnick, B. A. & Gayme, D. F. 2025 Restricted nonlinear simulations of flow over riblets: Characterizing drag reduction and its breakdown. *Int. J. Heat Fluid Flow* **116**, 109862.